

Scientific council of Faculty of Electrical  
Engineering and Information Technology

Slovak University of Technology in  
Bratislava

**Ing. Milan Kapolka**

**Three-dimensional electromagnetic  
modelling of practical superconductors  
for power applications**

**Summary of doctoral dissertation**

A dissertation submitted for the degree of  
Philosophiae Doctor in doctoral study programme:  
**5.2.48 Physical Engineering**

Bratislava 2018



This thesis was developed in a full-time doctoral study at Institute of Electrical Engineering, Slovak Academy of Sciences in Bratislava.

Author: Ing. Milan Kapolka

IEE SAS, Dúbravská cesta 9, 841 04 Bratislava

Supervisor: Mgr. Enric Pardo, PhD

IEE SAS, Dúbravská cesta 9, 841 04 Bratislava

Opponents: doc. RNDr. Tomas Plecenik, PhD

D.Sc. Antti Stenvall.....

.....

.....

.....

.....

Thesis summary was submitted on .....

Date of PhD thesis defence .....

Committee for dissertation defence in the doctoral study programme is appointed by chairman of joint study programme committee on .....

Code of programme: 5.2.48, doctoral study programme: Physical Engineering

Chairman of joint study programme committee: .....

# Contents

<b>1</b>	<b>Introduction</b>	<b>2</b>
<b>2</b>	<b>Theoretical method</b>	<b>3</b>
2.1	Sectors and parallel programming . . . . .	6
<b>3</b>	<b>Model tests</b>	<b>7</b>
3.1	Comparison of thin film model with analytical formulas. . . . .	7
3.2	Coupling effects in two-filament tape and measurements . . . . .	10
<b>4</b>	<b>Results and discussion</b>	<b>12</b>
4.1	3D Magnetization currents in rectangular prisms with constant $J_c$ . . . . .	12
4.2	Effect of aspect ratio of rectangular prisms . . . . .	13
4.3	Magnetization loops and penetration field of rectangular prisms with constant $J_c$ . . . . .	17
4.4	Cross-field demagnetization of cubes. . . . .	19
4.5	Anisotropic force-free effects in thin films . . . . .	23
4.6	Prism with various thicknesses and anisotropic force-free effects . . . . .	28
<b>5</b>	<b>Conclusion</b>	<b>32</b>

# 1 Introduction

The discovery of high-temperature superconductors with following research of many materials, such as REBCO and  $\text{MgB}_2$ , opened the door for superconducting power applications such as generators [1], motors [2], transformers [3], fault current limiters [4] and power transmission lines [5]. Superconductors are also widely used in large-bore magnets. Superconducting materials offer higher current density and magnetic field compared to normal conductors, and hence they improve the properties of large scale applications. However, they need to be cooled down below a certain critical temperature  $T_c$ . The cryogenic system is inefficient at low temperatures such as liquid helium or liquid nitrogen, and hence the AC loss presented by superconductors is often not feasible for superconducting power applications.

It is possible to reduce the AC loss by optimizing the configuration of the superconducting parts, and thence reach feasible superconducting power applications. The modelling methods can predict the properties of superconducting materials. However, 2D cross-sectional models cannot include finite size effects in finite samples or many power applications. There are several formulations of modelling methods but they are lacking of the required calculation speed and the accuracy for the full 3D situations. Therefore, full 3D modelling methods are required.

The modelling method has to handle a huge number of degrees of freedom in 3D mesh, in order to reveal all finite size effects. Further, the model result needs to be accurate with the measurements.

This thesis dissertation aims to develop a new variational

method to model the electromagnetic response of superconducting materials in 3D. The new formulation is implemented in a self-programmed tool written in C++ language with parallel computing ability. The modelling results are compared with analytical predictions and measurements, in order to verify their correctness. We study coupling effects in striated tapes, magnetization of rectangular prisms and cross-field demagnetization of cubic bulks. New findings are studied and discussed. Later, the findings are confirmed by measurements and other modelling methods.

## 2 Theoretical method

The modelling method is based on a variational principle with a new  $\mathbf{T}$  formulation defined as the effective magnetization, where the current density follows  $\mathbf{J} = \nabla \times \mathbf{T}$ . We name the method as the Minimum Electro Magnetic Entropy production (MEMEP 3D). The MEMEP 3D core is the 3D functional

$$\begin{aligned}
 L[\Delta\mathbf{T}] &= \int_V dV \left( \nabla \times \Delta\mathbf{T} \cdot \frac{(\Delta\mathbf{A}_a + \Delta\mathbf{A}_t)}{\Delta t} + U(\mathbf{J}_0 + \Delta\mathbf{J}_t + \nabla \times \Delta\mathbf{T}) \right) \\
 &+ \int_V dV \int_V dV' \frac{\mu_0}{8\pi\Delta t} \frac{(\nabla \times \Delta\mathbf{T}) \cdot (\nabla' \times \Delta\mathbf{T}')}{|\mathbf{r} - \mathbf{r}'|}, \quad (1)
 \end{aligned}$$

which has to be minimized [6], where  $\mathbf{A}_a$  is the applied vector potential,  $\mathbf{A}_t$  is the vector potential created by the transport current density  $\mathbf{J}_t$ ,  $\mathbf{J}_0$  is the current density in the time  $t_0$ ,  $\Delta t$  is the change of the time step and  $U$  is the dissipation factor

defined as

$$U(\mathbf{J}) \equiv \int_0^{\mathbf{J}} d\mathbf{J}' \cdot \mathbf{E}(\mathbf{J}'). \quad (2)$$

The solution of the functional is the same as the solution of the Maxwell differential equations, which is proofed by the Euler equations at the functional minimum. The second variation of the functional proofs that the solution is a minimum and unique.

A new minimization algorithm is developed as a part of the dissertation thesis, in order to reach short computing time.

We assume the  $\mathbf{E}(\mathbf{J})$  relation of the isotropic power law, which is

$$\mathbf{E}(\mathbf{J}) = E_c \left( \frac{|\mathbf{J}|}{J_c} \right)^n \frac{\mathbf{J}}{|\mathbf{J}|}, \quad (3)$$

where  $J_c$  is the critical current density,  $E_c$  is the critical electric field and  $n$  is the power law exponent depends on the superconducting material.

We also use the anisotropic power law

$$\mathbf{E}(\mathbf{J}) = 2m_0U_0 \left[ \left( \frac{J_{\parallel}}{J_{c\parallel}} \right)^2 + \left( \frac{J_{\perp}}{J_{c\perp}} \right)^2 \right]^{m_0-1} \cdot \left( \frac{J_{\parallel}}{J_{c\parallel}^2} \mathbf{e}_{\parallel} + \frac{J_{\perp}}{J_{c\perp}^2} \mathbf{e}_{\perp} \right), \quad (4)$$

where  $J_{c\perp}$  is the perpendicular critical current density,  $J_{c\parallel}$  is the parallel critical current density,  $m_0 = (n + 1)/2$ ,  $U_0 = E_c J_{c\perp} / (n + 1)$ ,  $J_{\parallel} = \mathbf{J} \cdot \mathbf{B} / |\mathbf{B}|$ ,  $J_{\perp} = |\mathbf{J} \times \mathbf{B}| / |\mathbf{B}|$  and  $\mathbf{e}_{\parallel}$ ,  $\mathbf{e}_{\perp}$  are unit vectors defined as  $\mathbf{e}_{\parallel} = \mathbf{B} / |\mathbf{B}|$  and  $\mathbf{e}_{\perp} = \mathbf{J}_{\perp} / |\mathbf{J}_{\perp}|$ .

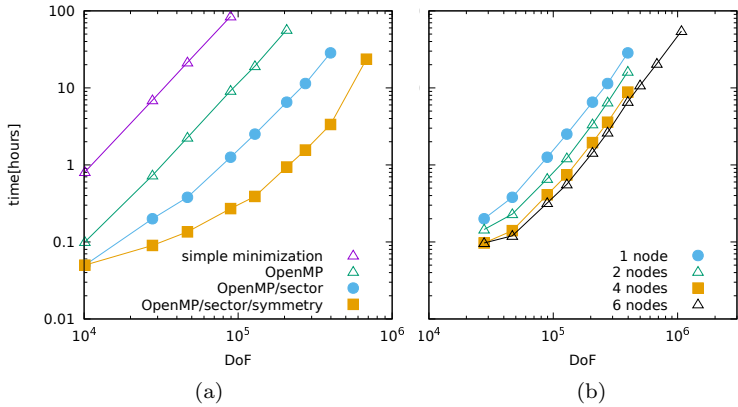


Figure 1: The calculation time of the MEMEP 3D modelling tool with increasing number of degrees of freedom and various sped up methods on (a) a single standard computer and (b) on a cluster. The model case is a cube with perpendicular applied field parallel to  $z$  axis and 10 time steps, in order to reach the peak of the applied field of 200 mT. The number of DoF in the symmetry corresponds to the full sample.

## 2.1 Sectors and parallel programming

The 3D mesh contains a huge number of elements, up to 1 million in our case, and hence the method needs to be sped up many times. The modelling tool includes parallel programming, in order to speed up the calculation time. The code uses two parallel programming protocols: Open MP on a single computer and BoostMPI multi-core CPU's protocol for a computer cluster.

The sample is divided into sectors, each being divided into smaller elements. Therefore, in the parallel computing each sector is solved by one thread. Thanks to the sectors, the efficiency of the parallel computing is high, around 90%. There are still some parts of the code calculated in series, and hence the parallel computing efficiency is not perfect.

The sectors speed up the minimization time around 8 times and the parallel computing another 8 times. The symmetry of the geometry reduces the minimization elements to  $1/8$ , and hence it speeds up the calculation time. The symmetry, if it is applicable, speeds up the minimization time by 7.5 times. In conclusion, all speed-up methods reduce the computing time by 2 or 3 orders as it is shown on figure 1(a).

The method includes as well parallel programming on the computer cluster with efficiency around 80%, since data transfer between the cluster nodes reduces the parallel efficiency. However, the cluster further reduces the computing time. The case of more than 1 million degrees of freedom takes around 55 hours on 6 cluster nodes [1(b)].

## 3 Model tests

### 3.1 Comparison of thin film model with analytical formulas.

The new calculation method has to show that the results are correct. Therefore, a basic example has been compared with analytical predictions such as a thin disk, as well as other cases [6]. The thin disk assumes the infinitely thin sheet approximation.

The modelling case is the electromagnetic response of the superconducting disk in the perpendicular applied field. The critical current density is  $2.72 \cdot 10^{10}$  A/m<sup>2</sup> with  $n$ -factor 1000. The radius of the disk is 6 mm and the thickness is 1  $\mu$ m. The instantaneous applied field is 7.8 mT parallel to  $z$  axis and with frequency 50 Hz. The current density slowly penetrates into the sample (2) and current lines follow the outer shape of the sample even though any cylindrical symmetry is not assumed. The hysteresis loop is compared with the analytical prediction (figure 3) with perfect agreement.

The solution of the isotropic power law with high  $n$  value is the same as the Critical State Model, which validates the MEMEP 3D method. The Critical State Model does not allow current densities higher than the critical current density, which is proved as well that for a thin disk there appear  $|\mathbf{J}| \leq J_c$ .

The MEMEP 3D method is further validated by comparison with other methods. Good agreement was found with the Finite Element Method (FEM) and Volume Integral Method (VIEM), for the case of tilted applied magnetic fields in prisms and stacks of tapes [8].

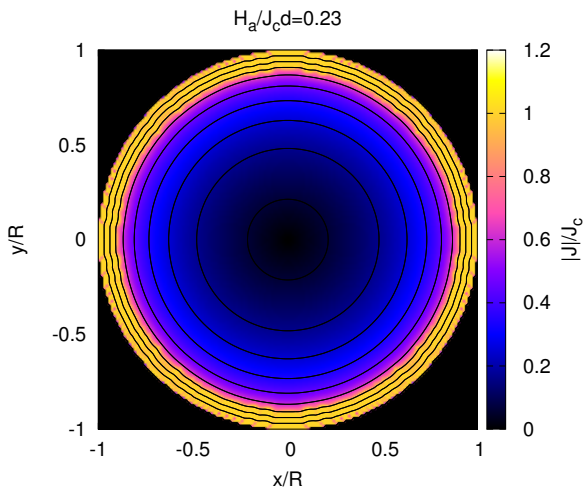


Figure 2: The modulus of the current density at applied field 7.8 mT for a thin disk. The current lines form circular loops, while the model does not assume any cylindrical symmetry.

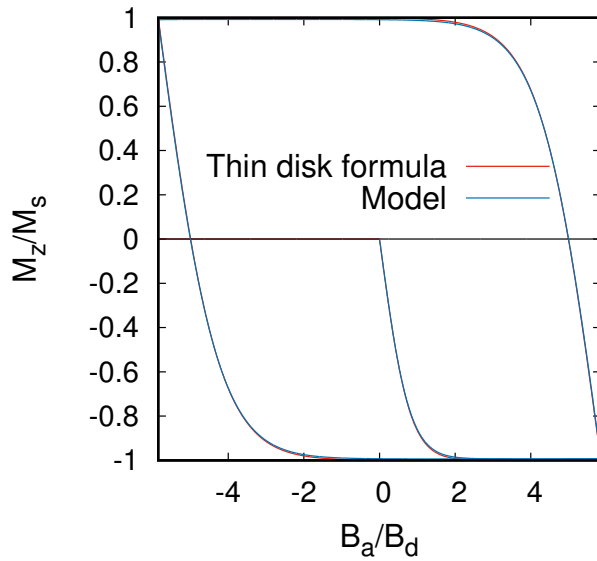


Figure 3: The thin disk magnetization loop agrees with the analytical formulas [7].

### 3.2 Coupling effects in two-filament tape and measurements

Another validation of the model is by measurements of the AC loss. The AC loss, and mainly the coupling loss, is important for High Temperature Superconductors, since the AC loss is high and increases with the tape width.

The measurement sample consists of two soldered superconducting tapes side by side of 22 mm length. The critical current of the 6 mm wide tape is 160 A. The applied field is perpendicular to the sample with applied field of 0.1-100 mT and with frequency 144 Hz. The AC loss is measured by the Calibration free method [9].

The model considers the same parameters as the measured sample. The power law uses an  $n$  factor of 30, which is a value closer to practical superconductors. The comparison between model and measurement is on figure 4 with very good agreement, with only 3% error. Deviation appears around 20 mT applied field, which is the self-field of the sample. The model assumes constant  $J_c$ . However, the model can include  $J_c(B)$ , and hence increase further the accuracy of the AC loss prediction. MEMEP 3D can model accurately AC loss in up to 10 filaments in the tape.

The measurements contain as well isolated non-soldered tapes of length 50 mm. Therefore, the measured AC loss per sample length is completely caused by hysteresis loss in the superconductor. The comparison of coupled and uncoupled cases shows that the coupling loss is dominant in low fields.

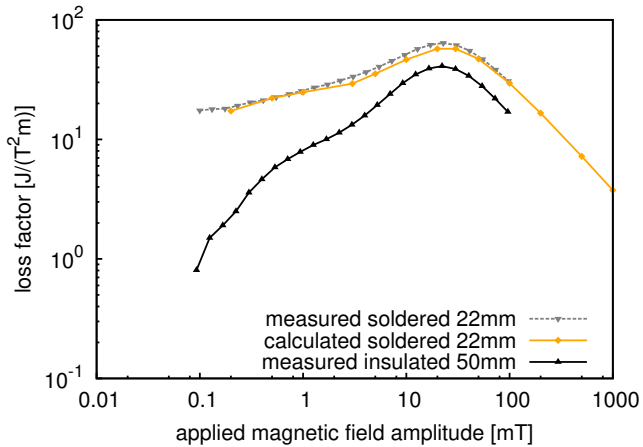


Figure 4: The AC loss factor, defined as the loss per cycle and length divided by the square of the applied field amplitude. Comparison of the measurements and model with two-tape conductor and frequency of the perpendicular applied field of 144 Hz. The calculations for the coupled case agree with the measurements.

## 4 Results and discussion

This Thesis results are focused on the electromagnetic response of superconductors in situations that are still not well understood. Superconducting bulks can generate higher magnetic fields than permanent magnets. However, the screening current of cubic samples is not well studied. The magnetization of prisms of several thicknesses reveals the intermediate state between the infinitely thin sheet approximation and infinite bar. Cross-field demagnetization is the real situation in motors, with rotating magnetic fields, and it predicts how long bulks remain magnetized in the motor. Most superconductors present force-free anisotropy. Therefore, a detailed study for this case is very important.

### 4.1 3D Magnetization currents in rectangular prisms with constant $J_c$

We study the magnetization of a cubic bulk and discuss the screening currents, which are still not well understood.

The modelling sample is a cubic bulk with edge of 10 mm and applied field parallel to the  $z$  axis with maximum amplitude of 200 mT. The sinusoidal applied field is with 50 Hz frequency. The critical current density is  $1 \cdot 10^8$  A/m<sup>2</sup> and the  $n$  factor is 100, which causes similar results to the Critical State Model.

The screening current density progressively penetrates into the sample when increasing the applied field to the peak. The bottom plane [figure 5(c)] is fully saturated by screening current density with round current lines at the center plane. The higher

cross-sectional planes show lower penetration depth [figure 5(b)]. The central cross-section presents a non-saturated zone with screening current and square current lines [figure 5(a)]. The model results show that cubic samples contain both types of current lines, square and round.

The calculation also reveals the  $J_z$  component of maximum value  $0.3J_c$ , which does not exist in cylindrical or fully saturated square samples.  $J_z$  is the highest in the diagonal lines [figure 5(e)]. The reason of the presence of  $J_z$  is that the cubic sample with square current lines cannot uniformly shield the applied magnetic field. At the corners, the self-field is too large. Therefore,  $J_z$  improves the shielding uniformly at the diagonal lines. The main screening current in the  $z$  plane is bended by the  $J_z$  component, as it is shown on the lateral surface [figure 5(d)]. Real 3D current lines are shown on figure 6.

## 4.2 Effect of aspect ratio of rectangular prisms

The study of aspect ratio effects on the rectangular prisms shows the intermediate state from the thin film approximation and infinite bar. The first part of the study is focused on the screening current path in the sample.

The modelling situation is the rectangular prism with the size of  $10 \times 10 \text{ mm}^2$  and thickness in the range of 1-20 mm. The sinusoidal applied field is parallel to the  $z$  axis with frequency of 50 Hz. The applied field is  $B_a = 0.484B_s$ , where  $B_a$  is the applied field and  $B_s$  is the saturation field for each aspect ratio. The critical current density is  $1 \cdot 10^8 \text{ A/m}^2$  and the  $n$  factor is 100. The aspect ratio  $c$  is defined as  $c = w/d$ , where  $w$  is the

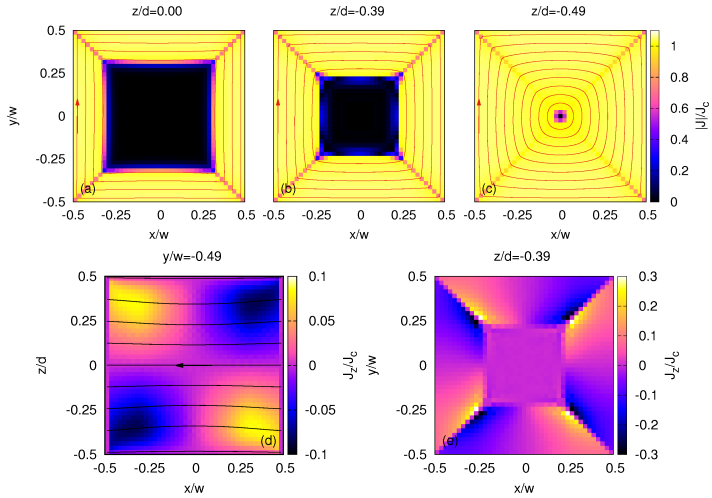


Figure 5: The penetration of current density modulus into the cube with power law  $n = 100$  at the peak of the applied field of 200 mT amplitude. The cross-sectional planes are at (a)  $z/d = 0$ , (b)  $z/d = -0.39$ , (c)  $z/d = -0.49$ , (d)  $y/w = -0.49$  and (e)  $z/d = -0.39$ .

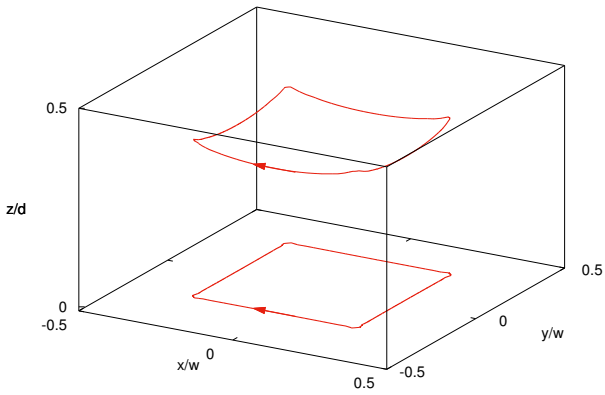


Figure 6: The upper half of the cube sample with real 3D current lines in two positions. The current lines are bended from  $z$  plane by  $J_z$  component, which improve shielding of the applied fields in corners.

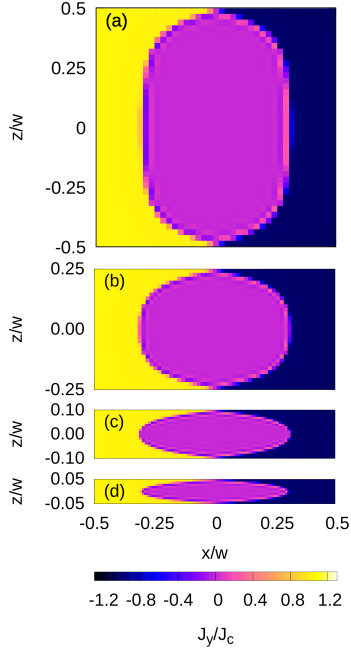


Figure 7: The  $J_y$  component of the current density in the mid plane  $y/w = 0$  for various aspect ratios  $c = w/d$  of the prism with  $n=100$  and the applied field of the same ratio  $B_a = 0.484B_s$ , where  $B_s$  is the saturation field defined in section 4.3. (a)  $c=1$ , (b)  $c=0.5$ , (c)  $c=0.2$ , (d)  $c=0.1$ . The penetration depth of  $J_y$  is the same for each case of  $c$ .

width of the sample and  $d$  is the thickness of the sample with values of  $c = 0.1, 0.2, 0.5, 1, 2$ .

The cross-sectional plane of the full 3D model at the mid plane  $y/w=0$  shows the  $J_y$  component of the current density on figure 7 for all aspect ratios. For  $c = 1$ , the current front close to the center is parallel to the  $y$  axis [figure 7(a)]. Thinner samples showed the same penetration depth, but with more squeezed non penetrated central zone [figure 7(b),(c),(d)]. The model proved that the current path is not changing with the decreasing thickness, and hence there exist non-zero  $J_z$  component of maximum value  $0.3J_c$  even in the case of  $c = 0.1$  [10]. We calculated as well the average current density over the thickness of the aspect ratio 0.1 [figure 8], where current lines qualitatively agree with the thin film model.

### 4.3 Magnetization loops and penetration field of rectangular prisms with constant $J_c$

The second part of the study is focused on the magnetization loops and penetration field with various aspect ratios  $c$ . The modelling situation is the same as the previous study of the screening current in the prism.

The hysteresis loops are on figure 9 with applied field 1 T. the hysteresis loops show that the saturation field is the smallest for the prism with  $c = 0.1$ , as it is expected for a thin film. However, an infinitely thin film saturates at an applied field with infinite value. The magnetization and the saturation field increases with thickness of the sample, since thicker samples can induce higher screening magnetic fields. The flat curve of the hysteresis loops

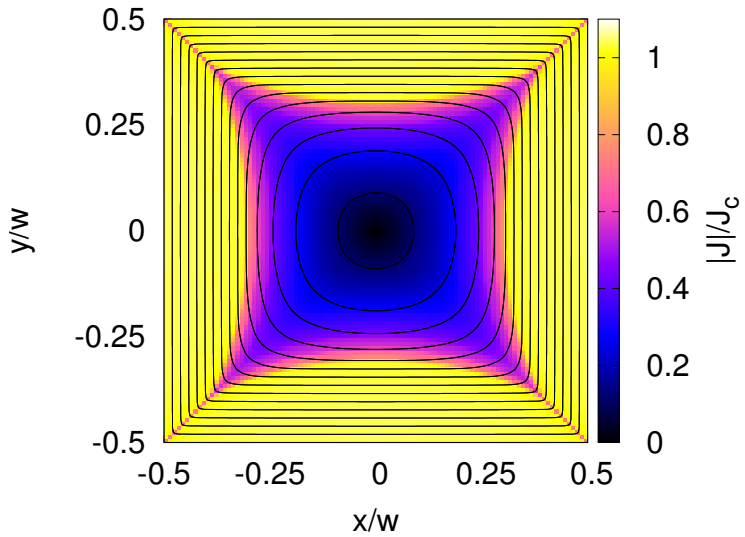


Figure 8: The average current density over the thickness of the prism with aspect ratio  $c = 0.1$ . The current distribution is qualitatively similar to the thin film.

at saturated state is caused by the high  $n$  factor of value 100, which does not allow  $|\mathbf{J}| > J_c$  as it is in the Critical State Model.

We set the saturation field as 99% of the magnetization of the sample, in order to unify all criterions for cylinder, slab and strip since the prism presents features of all of them. The saturation field  $M(B_s) = 0.99M_s$  on aspect ratio  $c$  is showed on figure 10 with analytical predictions for infinite thin film and infinite bar. Our analytical fit reached 97% accuracy, reaching as well the thin film and bar limits. The analytical fit is

$$B_s(c) = \mu_0 J_c w a_1 \left[ 1 + a_2 e^{\frac{-\ln^2(a_3 c)}{2a_4^2}} \right] \tanh(a_5 c), \quad (5)$$

where the fit parameters are  $a_1 = 0.3915$ ,  $a_2 = -0.26$ ,  $a_3 = 2.56$ ,  $a_4 = 0.75$  and  $a_5 = 2.41$ .

#### 4.4 Cross-field demagnetization of cubes.

The cross-field demagnetization is important, since the same situation appears in the motor, where rotating magnetic fields demagnetize the rotor.

The modelling situation is divided into two steps: the first part is magnetization of the sample, followed by relaxation without any applied field. The second part is the demagnetization of the sample with applied cross-fields. The cubic sample is of 6 mm edge size with  $J_c = 2.6$  A/m<sup>2</sup> and  $n$  of 30. The maximum magnetizing applied field is 1.3 T parallel to the  $z$  axis. This magnetization field is with triangular waveform and ramp rate 13 mT. The modelling method uses the Field Cooled method,

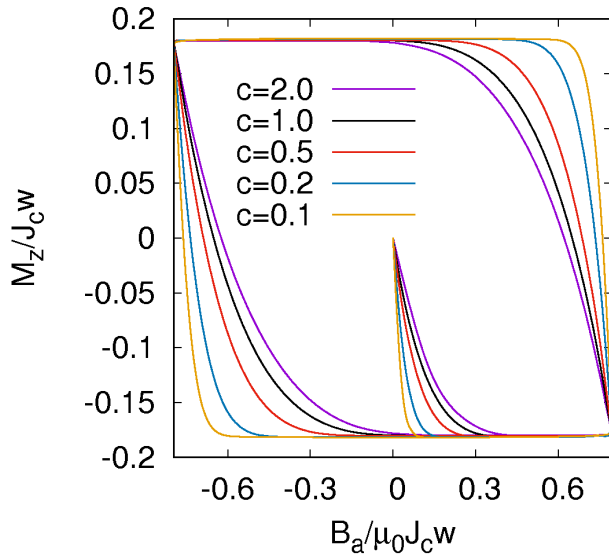


Figure 9: The hysteresis loops of the prisms with various aspect ratio  $c = d/w$  and the applied field amplitude of 1 T. The saturation field increases with aspect ratio  $c$ .

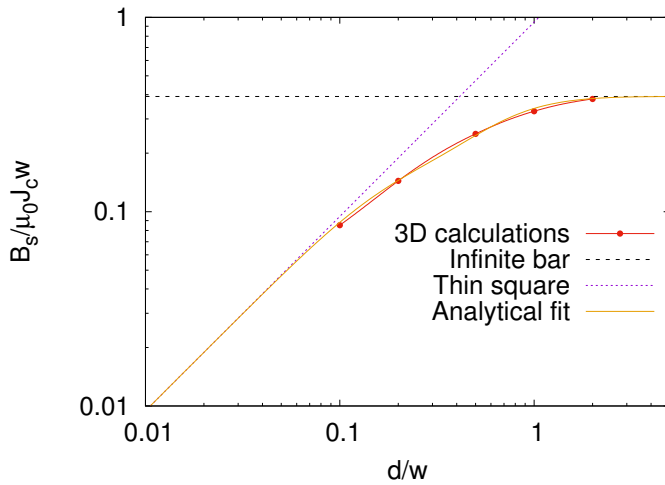


Figure 10: The saturation field increases with on the aspect ratio  $c = d/w$ . The analytical fit of equation (5) reaches 97% accuracy and meets the thin square and infinite bar limits.

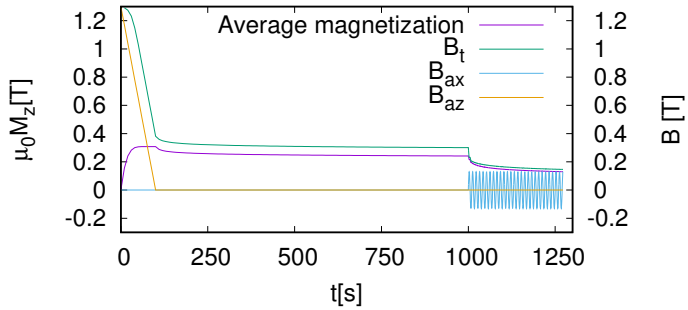


Figure 11: The figure of the entire magnetization and demagnetization process over time with wave-forms of the applied field  $B_{az}$  and ripple  $B_{ax}$ . The magnetization inside the sample and trapped field at  $100 \mu m$  above the sample are reduced by the applied ripples.

followed by 900 s of relaxation time. The cross-field, parallel to the  $x$  axis, is with amplitude of 130 mT and frequency 0.1 Hz. The entire demagnetization process is on the figure 11 with average magnetization and trapped field. The trapped field is 100  $\mu\text{m}$  above the sample surface at the middle of the  $z$  plane.

The usual peak of the trapped field at the end of the relaxation time is on figure 12 with black curve. The trapped field profile is along the  $x$  axis, parallel to the cross-field direction. The first peak of the cross-field reveals the asymmetry of the trapped field [figure 12, blue curve]. The peak of the trapped field decreases and it is shifted to the left. The next minus peak of the cross-field shifts the trapped peak back to the center [figure 12, red curve]. The origin of the asymmetry is the screening current inside the bulk sample, which creates an “S” shaped current profile [11]. The asymmetry was confirmed by another 3D method [12], as well as by measurements. The demagnetization of the bulk measurements agree very well with the model predictions [figure 13]. However, calculations for the highest cross-fields, present inaccuracies. Higher accuracy can be reached by taking the real value of the power law exponent of the sample and including the  $J_c(B)$  dependence.

## 4.5 Anisotropic force-free effects in thin films

Most superconductors present force-free anisotropy, a fundamental study of the thin film anisotropy is of high interest. The force-free effects appear when the current density  $\mathbf{J}$  is not perpendicular with the local magnetic field  $\mathbf{B}$ , often involving vortex breaking and cutting.

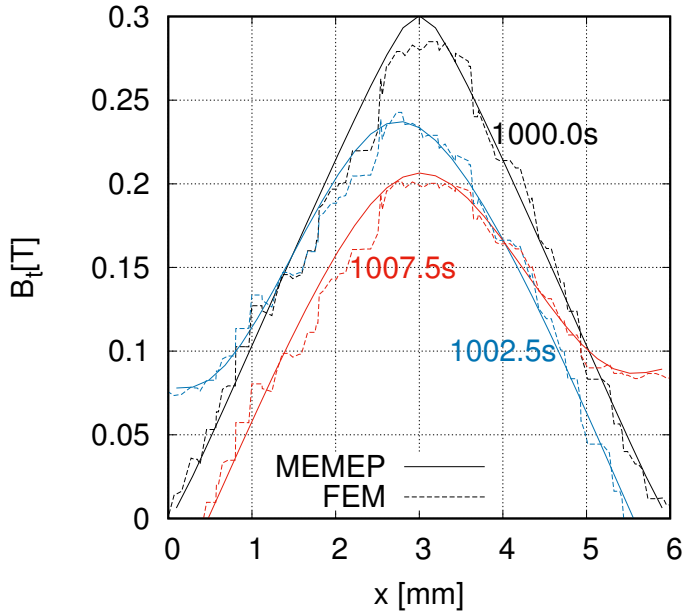


Figure 12: The peak of the trapped field at the end of the relaxation time of 900 s, which follows the 100 s long magnetization by  $B_{az}$ . The blue and red lines are trapped fields at 1002.5 s (at first positive peak of ripple) and 1007.5 s (at first negative peak of ripple).

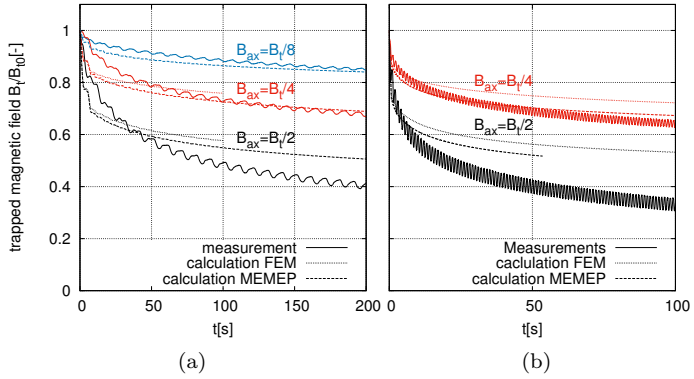


Figure 13: The comparison of the cube demagnetization by cross-field  $B_{ax}$  measurements with the MEMEP 3D and FEM models. The measurements with ripples of (a) 0.1 Hz and (b) 1 Hz. The models and measurements agree for low ripple amplitudes.

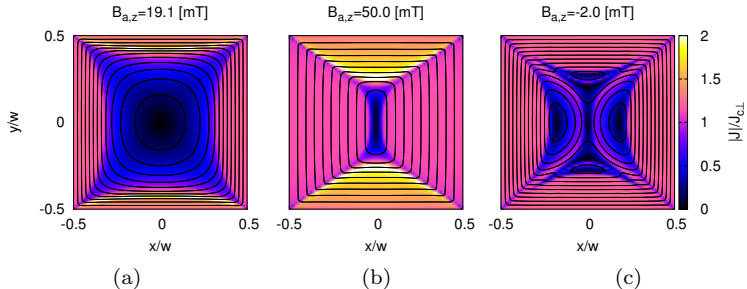


Figure 14: The gradual penetration of the current density into the anisotropic thin film with the sinusoidal applied field amplitude  $B_a=70.7$  mT. The applied field angle is  $\theta=45^\circ$ .

The geometry of the study is a thin film of size  $12 \times 12$   $\text{mm}^2$  and thickens  $1 \mu\text{m}$ . The perpendicular critical current density is  $3 \cdot 10^{10}$   $\text{A}/\text{m}^2$  and the parallel critical current density is  $J_{c\parallel} = 3J_{c\perp}$ . The power law  $n$  value is 30 and the sinusoidal magnetic field amplitude is 50 mT. The applied field angle  $\theta$  is in the range of  $0-80^\circ$  with constant  $z$  component of the applied field.

The screening current of the case of  $\theta = 45^\circ$  is on figure [14(a)]. The maximum  $J_y$  component of the current density is with value around  $J_{c\perp}$  (regions close to the right and left edges). However, the  $J_x$  component reaches a value around  $2J_{c\perp}$  (regions close to the top and bottom edges), since  $J_x$  is more aligned with the direction of the applied field, and hence  $J_{c\parallel}$  is involved. The

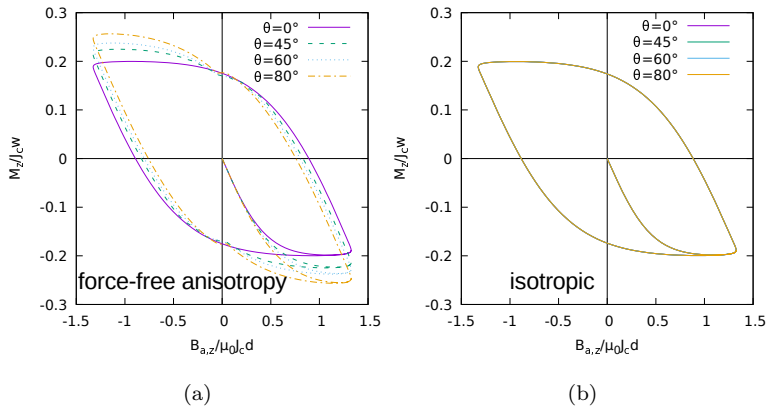


Figure 15: The magnetization loops with (a) anisotropic and (b) isotropic power law. The sinusoidal applied field amplitude is of  $B_{a,z}=50$  mT with frequency of 50 Hz and  $n$  value 30.

penetration depth is lower than for  $J_y$ , because of the higher current density. The peak of the applied field shows the same penetration behavior and the sample is almost fully saturated [figure 14(b)]. The remanent state shows the reduction of the “enhanced”  $J_x$  component, since the applied field is zero and the self-field is perpendicular to the current density direction [figure 14(c)].

The hysteresis loops for the anisotropic power law in the thin film are on figure 15(a). The magnetization increases with the angle, since the alignment of the current density with the applied field increases the value of  $|\mathbf{J}|$  to  $J_{c\parallel}$ . However, the isotropic case of the same applied field angles presents constant magnetization for all angles, since there is always  $|\mathbf{J}| \approx J_{c\perp}$ . For the anisotropic case, there appears a minimum at the remanence. The cause is that at the remanence the local magnetic field is always perpendicular, reducing  $|\mathbf{J}|$  to  $|J_{c\perp}|$ .

## 4.6 Prism with various thicknesses and anisotropic force-free effects

The second anisotropy study of the force-free effects is on the prism with various applied field angles  $\theta$ .

The prism sample is of the size  $12 \times 12 \text{ mm}^2$  and with thickness of 1 mm. The perpendicular critical current density is  $3 \cdot 10^7 \text{ A/m}^2$  and  $J_{c\parallel} = 3J_{c\perp}$  with power law  $n$  value 30. The modelling case with applied field amplitude 100 mT and angle  $\theta = 60^\circ$ .

The current density of the thin film and prism agree very well, even though the prism contains less elements in each  $z$  plane. However, the prism model is a full 3D model with higher

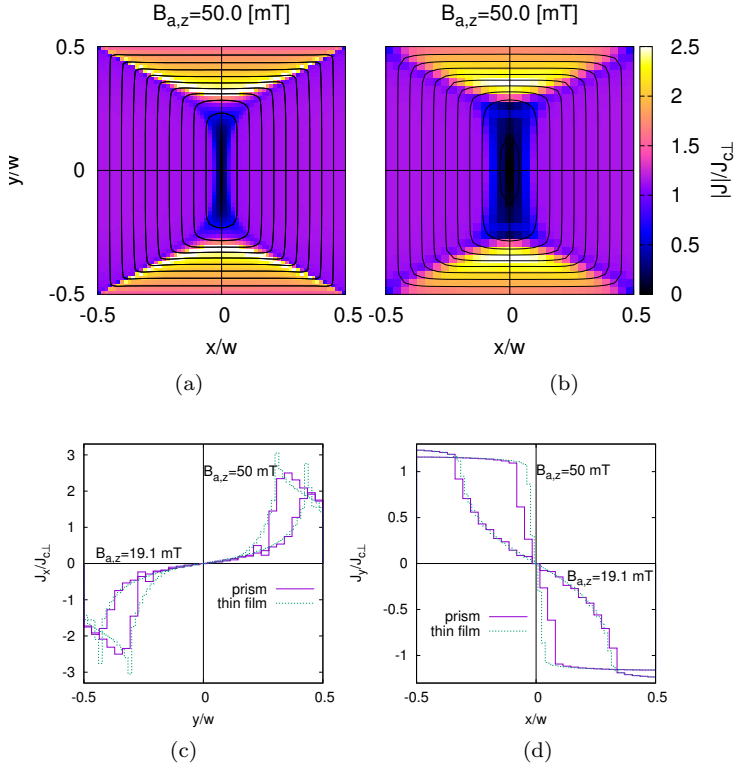


Figure 16: The penetration of the thickness-average current density at the peak of applied field of 100 mT with angle  $\theta = 60^\circ$  in (a) thin film and (b) prism. The current density in the mid cross-section is shown for the (c)  $J_x$  and (d)  $J_y$  components.

total number of elements, having several elements in the  $z$  direction. The average current density over the thickness is calculated [figure 16(b)] and compared with the thin film case [figure 16(a)]. The current penetration is qualitatively the same. The  $J_x$  component is the highest at the penetration front, where the perpendicular self-field vanishes, and hence  $|\mathbf{J}|$  is not reduced to  $J_{c\perp}$ .

A closer comparison with the cross-sectional planes at  $y/w = 0$  and  $x/w = 0$  of the  $J_x$  and  $J_y$  components is shown on figures 16(c),(d). The  $J_y$  component of both samples show the same penetration depth [figure 16(d)] with slightly lower penetration depth of the prism at the peak of applied field, caused by coarser mesh in the  $z$  plane. The  $J_x$  comparison shows as well the same penetration depth of both samples [figure 16(c)]. However, the thin film with narrower cells presents a higher peak of the penetration front of the current density.

The hysteresis loops show a peak after the remanent state [figure 17(a),(b)]. The cause is that for a prism, there is also a parallel component of the self-field. Then, at remanence there appears zones with “enhanced” current density, in addition to these caused by a tilted applied field. The  $M_x$  magnetization increases with the applied field angle  $\theta$ , since the current density can flow in the  $z$  direction and the average plane of the current loops is tilted by the applied field angle. The  $M_z$  component depends on two aspects. The magnetization decreases with the applied field angle because of the tilted screening current density but also increases because of the alignment of the current density and local magnetic field, which increases the current density to the value of  $J_{c\parallel}$ .

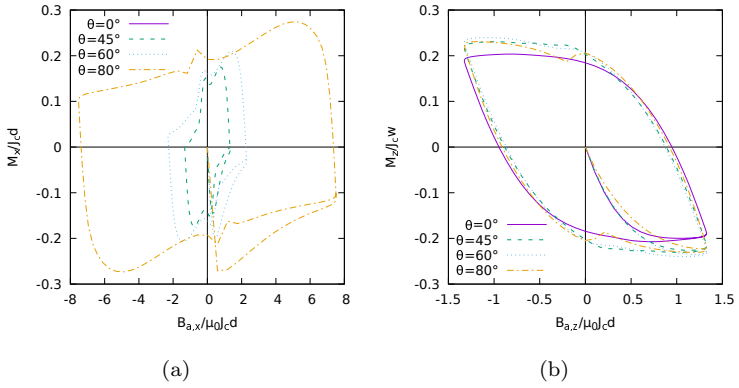


Figure 17: The magnetization loops with anisotropic power law and various angles  $\theta$  of the applied field. The magnetization components (a)  $M_x$  and (b)  $M_z$  are shown.

## 5 Conclusion

Since High Temperature superconductors are non-linear materials, powerful mathematical models are required. Superconducting power application machines are of finite size, and hence 2D cross-sectional models are not enough to explain all finite size effects. Therefore, 3D modelling methods are needed with fast calculation time to handle full 3D meshes with a lot of elements, and providing accurate predictions. 3D modelling tools with possibility of many dependences like anisotropy and  $J_c(B)$  are the most promising, in order to reach high agreement with measurements.

This PhD thesis developed a new variational method based on the  $\mathbf{T}$  effective magnetization, called Minimum Electro Magnetic Entropy Production (MEMEP) 3D. The modelling tool is programmed in the C++ language with parallel programming structure. The parallel programming efficiency reached 80% on computer cluster and allows to model samples with more than 1 million degrees of the freedom in less than 55 hours.

The results of MEMEP 3D are verified with the 2D analytical predictions and also with the measurements of the AC loss on a 2 filaments tape with only 3% error. Another important result is the magnetization current density in the cube sample, which was previously not well understood. The model revealed non-zero  $J_z$  component and explained the full 3D current path. Afterwards, we showed the screening current path in prisms with different thickness, which confirmed not vanishing  $J_z$  component even at aspect ratio 0.1. The analytical fit of the penetration field as a function of the aspect ratio of the rectangular prism reached the

accuracy of the 97%. The fit allows to predict the penetration field of any aspect ratio between the thin film approximation and the infinite bar.

Our 3D calculations of the screening current of the cube was chosen as benchmark model in the international HTS modelling workshop 2016. This was followed by cooperation with the comparison of three modelling methods by tilted applied fields in prisms and stacks of the tapes [13]. The comparison further validated the MEMEP 3D method. Detailed cross-field demagnetization study of the cube showed very good agreement with measurements and other 3D methods. The demagnetization case is very important for the case of rotating fields, like in the motor.

The anisotropy study showed the prediction of the screening currents and hysteresis loops in thin films and prisms with tilted applied fields based on the Elliptical Critical State Model. This physical model describes force-free effects, resulting in anisotropic  $\mathbf{E}(\mathbf{J})$  relation. The detailed study is important, since most superconductors present this kind of anisotropy.

In the conclusion, the MEMEP 3D method proofed to be a very useful method with fast calculation time and accuracy. The results are confirmed by other 3D modelling methods and measurements. The results found new superconducting effects. The method can potentially improve superconducting power applications.

## References

- [1] SUPRAPOWER-EU project. Superconducting light generator for large offshore wind turbines. <http://www.suprapower-fp7.eu/>.
- [2] T. Yanamoto, M. Izumi, K. Umemoto, T. Oryu, Y. Murase, and M. Kawamura, “Load test of 3-MW HTS motor for ship propulsion,” *IEEE Trans. Appl. Supercond.*, vol. 27, no. 5204305, 2017.
- [3] S. Hellmann, M. Abplanalp, L. Hofstetter, and M. Noe, “Manufacturing of a 1-MVA-Class superconducting fault current limiting transformer with recovery-under-load capabilities,” *IEEE Trans. Appl. Supercond.*, vol. 27, no. 5500305, 2017.
- [4] T. Pascal, A. Badel, G. Auran, and G. Pereira, “Superconducting fault current limiter for ship grid simulation and demonstration,” *IEEE Trans. Appl. Supercond.*, vol. 27, no. 5601705, 2017.
- [5] E. Volkov, V. Vysotsky, and V. Firsov, “First russian long length HTS power cable,” *Physica C-Superc. and its apl.*, vol. 482, pp. 87–91, 2012.
- [6] E. Pardo and M. Kapolka, “3D computation of non-linear eddy currents: variational method and superconducting cubic bulk,” *J. Comput. Phys.*, vol. 344, pp. 339–363, 2017.

- [7] J. Clem and A. Sanchez, “Hysteretic ac losses and susceptibility of thin superconducting disks,” *Phys. Rev. B*, vol. 50, no. 13, p. 9355, 1994.
- [8] E. Pardo, J. Šouc, and L. Frolek, “Electromagnetic modelling of superconductors with a smooth current-voltage relation: variational principle and coils from a few turns to large magnets,” *Supercond. Sci. Technol.*, vol. 28, p. 044003, 2015.
- [9] J. Šouc, F. Gömöry, and M. Vojenčiak, “Calibration free method for measurement of the ac magnetization loss,” *Supercond. Sci. Technol.*, vol. 18, no. 5, p. 592, 2005.
- [10] E. Pardo and M. Kapolka, “3D magnetization currents, magnetization loop, and saturation field in superconducting rectangular prisms,” *Supercond. Sci. Technol.*, vol. 30, no. 064007, p. 11, 2017.
- [11] A. Campbell, M. Baghdadi, A. Pafel, D. Zhou, K. Y. Huang, Y. Shi, and T. Coombs, “Demagnetisation by crossed fields in superconductors,” *Supercond. Sci. Technol.*, vol. 30, 2017.
- [12] M. Kapolka, V. M. R. Zermeno, S. Zou, A. Morandi, P. L. Ribani, E. Pardo, and F. Grilli, “Three-dimensional modeling of the magnetization of superconducting rectangular-based bulks and tape stacks,” *IEEE Trans. Appl. Supercond.*, vol. 28, no. 8201206, 2018, DOI: 10.1109/TASC.2018.2801322.

- [13] M. Kapolka, J. Srpic, D. Zhou, M. Ainslie, E. Pardo, and A. Dennis, "Demagnetization of cubic gd-ba-cu-o bulk superconductor by cross-fields: measurements and 3d modelling," *IEEE Trans. Appl. Supercond.*, vol. 28, no. 6801405, 2018, doi: 10.1109/TASC.2018.2808401.